Research Article

Rabie Dehane, Khatir Naima, Abdelkrim Liazid, Mustafa Inc*, Abdallah Benarous, Hijaz Ahmad, and Younes Menni*

Impact of the convergent geometric profile on boundary layer separation in the supersonic over-expanded nozzle

https://doi.org/10.1515/phys-2022-0185
received March 18, 2022; accepted June 16, 2022

Abstract: This article aims to conduct a numerical investigation of phenomena induced by gas expansion in chemical propulsion nozzles. A numerical simulation of full-scale flat convergent-divergent nozzle geometry using the finite volume method on structured meshes is performed to predict the change in the convergent geometry on the boundary layer separation resulting from a shock/shock and shock/boundary layer. Two turbulence models are tested, namely, the k–ε and k–ω shear-stress transport (SST) models. Three steps are considered to achieve this work. First, 10 numerical schemes are tested to select the accurate one. The findings of the first step are used to predict the boundary layer separation in a supersonic overexpanded nozzle. The available experimental data from the NASA Langley Research Center are used to validate the results. The third step concerns investigating the impact of the convergent geometric profile on the downstream flow of the nozzle. The obtained results are analyzed and compared with the experimental data. These results show that convergent geometry may cause the formation of different shock structures and different points of flow separation and modifies several parameters of the flow and nozzle performance downstream the throat. The findings indicated that the convergent profile must be considered during the design phase when focusing on the problem of boundary layer separation in the supersonic overexpanded regime nozzles.

Keywords: lateral load, separation criterium, shock tube, plan convergent divergent nozzle, Riemann problem

*** Corresponding author: Mustafa Inc,** Department of Computer Engineering, Biruni University, Istanbul, 34025, Turkey; Department of Mathematics, Science Faculty, Firat University, Elazig, 23119, Turkey; Department of Medical Research, China Medical University Hospital, China Medical University, Taichung 40402, Taiwan, e-mail: minc@firat.edu.tr
*** Corresponding author: Younes Menni,** Department of Technology, University Center Salhi Ahmed Naama (Ctr. Univ. Naama), P.O. Box 66, Naama, 45000, Algeria, e-mail: menni.younes@cuniv-naama.dz
Rabie Dehane: Department of Mechanical Engineering, Faculty of Technology, Hassiba BenBouali University of Chlef, Ouled Fares, P.O. Box 151, 02000, Chlef, Algeria
Khatir Naima: Department of Technology, University Center Salhi Ahmed Naama (Ctr. Univ. Naama), P.O. Box 66, Naama, 45000, Algeria
Abdelkrim Liazid: Department of Physics, Faculty of Technology, Abou Bekr Belkaid University, 22 Rue Abi Ayed Abdelkrim, 13000, Tlemcen, Algeria
Abdallah Benarous: Department of Mechanical Engineering, Faculty of Technology, University of Saàd Dahlab Blida, P.O. Box 270, 09000, Blida, Algeria
Hijaz Ahmad: Section of Mathematics, International Telematic University Uninettuno, Corso Vittorio Emanuele II, 39, 00186 Roma, Italy

Nomenclature

A	section
e	internal energy
E	total energy
N	number of intervals
P	pressure
R	constant of the gas
S	term source
T	temperature
t	time
u	velocity
x	abscissa
Y	Coordinates
γ	adiabatic index
ρ	density
φ	the flux vector
ω	the vector of the conservative variables

Indices

0	generative condition
a	inlet
amb	ambient
s	outlet
sep	separation
t	nozzle throat

Abbreviations

AUFS	artificially upstream flux vector splitting
AUSM	advection upwind splitting method
HLL	Harten, Lax et van Leer
Mach	Mach number
NPR	nozzle pressure ratio

1 Introduction

Predicting flow separation in supersonic overexpanded nozzles resulting from a shock/boundary–layer interaction represents a significant stake in aerospace science [1]. The prediction allows the control of this phenomenon and develops in rocket nozzles. Indeed, during the thermal energy conversion into kinetic energy inside the convergent-divergent nozzle, an overexpanded flow process is needed to obtain the maximum power [2]. This expansion induces an increase in gas momentum and simultaneously a significant decrease in pressure and temperature, which causes a shock wave formation [3]. Due to the flow aeroelastic characteristics and the interaction of the shock waves with the boundary layer, a phenomenon of flow separation is generated [4]. The boundary layer separation causes a recirculation zone (reintroduction of ambient air) between the wall and the external environment and detached flow. This zone may give uncontrolled lateral loads [5]. Therefore, closer is a separation point to the nozzle outlet lip, the more a recirculation zone formation is avoided [6].

Several studies [7–9] were performed experimentally on subscale and full-scale models to demonstrate and understand the relation between the shock wave and boundary layer, notably how to cause the separation flow in an overexpanded nozzle [10,11].

The previous studies [12,13] revealed the existence of two different patterns of separation defined as the free shock separation (FSS) and restricted shock separation (RSS). In the case of FSS, flow/wall separation continued until the exit of the nozzle. While in RSS, the flow is reattached to the wall downstream of the separation location [5,14,15]. Papamoschou *et al.* [16] achieved an experimental investigation on the supersonic case with a planar converging–diverging nozzle where the geometry is flexible with variable nozzle pressure ratio (NPR). They pointed out that the section ratio $A_s/A_t > 1.2$ and the ratio NPR > 1.4 have a decisive impact on creating the shock wave and boundary layer separation. Gouidmi *et al.* [17] carried out a numerical study on the influence of the boundary layer profile and separation and the behavior of the flow in front of shock–the boundary layer interaction. Quadros and Bernardini [18] conducted a numerical investigation on the transitional shock wave–boundary layer interaction in the supersonic regime. It was found that the extent of the interaction region and properties are highly affected by the regime of the incoming flow. Meister *et al.* [19] studied the external nozzle parameters, precisely the parietal temperature and the ambient airflow velocity around the nozzle. They pointed out that the outward flow velocity causes the thickening of the mixed layer in the recirculation zone, which remains in contact with the nozzle wall during the stationary phase. This phenomenon is due to the thermal stress on the nozzle wall. Genin and Stark [20] studied the influence of the divergent geometry (dual bell nozzle) on boundary layer separation. They concluded that the extension length is the principal parameter for optimizing the flow behavior and side-load generation.

In reviewing the literature, the prediction and the understanding of the impact of the different parameters on the apparition and behavior of the flow separation in overexpanded supersonic convergent–divergent nozzle geometry remain a significant research gap. However, it is now well established that geometry, especially divergent parts, impacts the flow separation apparition. However, the influence of convergent geometry has remained unclear and not fully understood.

This study aims to contribute to this growing research field by focusing on three main axes: (1) to verify that the convergent geometry impacts the boundary layer separation, (2) to define the effects of this parameter on flow and separation behavior, and (3) determine the importance of convergent geometry change on the flow behavior, apparition of flow separation, and the nozzle's performance.

To perform this study, different numerical schemes are tested in a shock tube case to select the best one to predict the boundary layer separation in a supersonic overexpanded nozzle. A series of experimental investigations on the NASA Langley Research Center 16-Foot Transonic Tunnel complex are performed to validate

the numerical simulation, and hence, a deep analysis of the impact of the convergent geometry on the flow separation phenomenon is performed.

2 Formulation of the shock tube problem

A diaphragm separates the shock tube in the middle, creating two zones with different thermodynamics states $P4 > P1$. When the diaphragm is broken, two shock waves appear. The first one is formed and propagated along the tube from a high-pressure zone to low-pressure one called a shock wave (recompression wave). The second shock wave is propagated in the opposite direction and is known as a relaxation wave. This configuration is called the Riemann problem, as shown in Figure 1.

The tube is considered to be sufficiently long to avoid a reflection effect. We also assume that these two regions (two sides separated by the diaphragm) contain the same gas and negligible viscous effects. The fluid is considered as an ideal gas under polytropic transformation and submitted to an expansion, leading to a variable velocity in the space-time (x, t) domain. When assuming the ideal gas assumption, Eq. (1), the Euler formulation can be described by the conservative equation of a variable (ω), as shown in Eq. (2).

$$p = \rho RT = (\gamma - 1)\rho\left(e - \frac{1}{2}u^2\right), \tag{1}$$

$$\frac{\partial \omega}{\partial t} + \frac{\partial}{\partial x}\varphi(\omega) = S(\omega), \tag{2}$$

where S represents the source term and (ω) denotes the vector of the conservative variables of mass, momentum, and energy, which can be expressed as follows:

$$\omega = \begin{pmatrix} \rho \\ \rho u \\ \rho E \end{pmatrix}. \tag{3}$$

The flow vector is given by:

$$\varphi(\omega) = \begin{pmatrix} \rho u \\ \rho u^2 + p \\ (\rho E + p)u \end{pmatrix}. \tag{4}$$

The computation domain is discretized in x_i intervals $(i = 1...N)$, where $N = \frac{l}{\Delta x}$ is the number of nodes and l is the length of the tube. The finite volume method is used to solve the conservation Eq. (2). It integrates the conservation laws on an elementary cell $(x_{i-1/2}, x_{i+1/2})$. In each cell, the vector of the conservative variables is assumed to be constant and can be expressed as follows:

$$\frac{\partial}{\partial t}\int_{x_{i-1/2}}^{x_{i+1/2}} \omega \mathrm{d}x + \int_{x_{i-1/2}}^{x_{i+1/2}} \frac{\partial \varphi(\omega)}{\partial x}\mathrm{d}x = \int_{x_{i-1/2}}^{x_{i+1/2}} S(\omega)\mathrm{d}x. \tag{5}$$

The final equation form at the integration time $t = n\,\Delta t$ is:

$$\Delta x \frac{\partial \omega_i^n}{\partial t} + \hat{\varphi}_{i+1/2}^n - \hat{\varphi}_{i-1/2}^n = \Delta x \bar{S}_i^n. \tag{6}$$

The previous study has proposed several numerical schemes [21] to predict the shock wave inside the tube

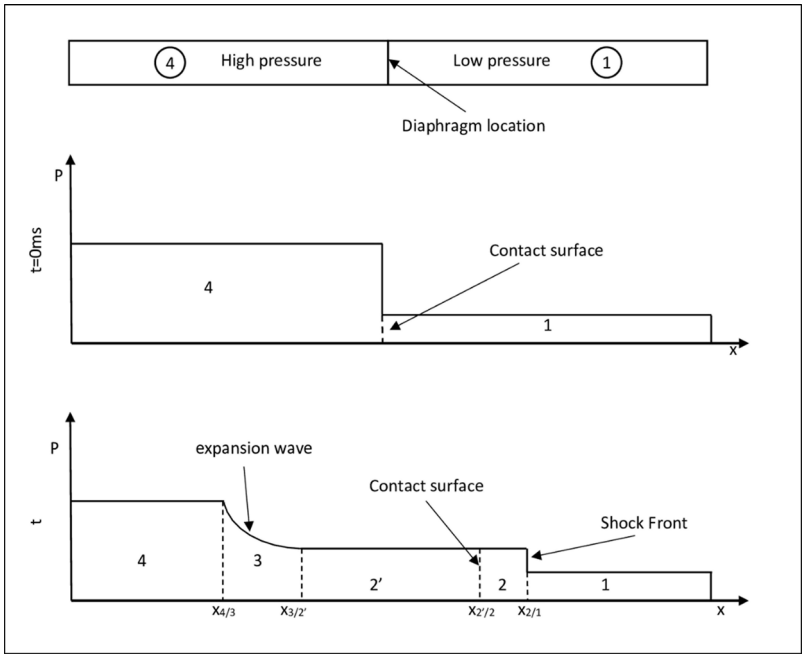

Figure 1: Schematic pressure distribution in the shock tube problem before and after diaphragm removal.

POINT	COORDINATES, IN. X	Y
A	0.000	0.000
B	0.000	-0.614
C	0.000	1.386
D	0.917	1.163
E	1.988	0.611
F	2.394	0.553
G	2.430	0.559
H	2.275	1.166
I	4.550	0.972

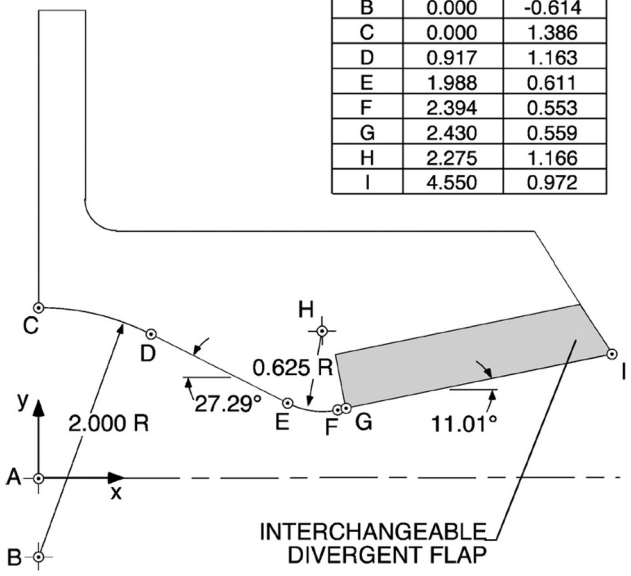

Figure 2: Presentation of the NASA nozzle geometry [25].

shock. The Riemann approximation solution [22–24] can be obtained by different schemes like Lax-Wendorf, centered scheme, scheme of decomposition flow, scheme type Riemann solver, and no oscillation scheme.

3 Numerical study of the selected NASA nozzle

Numerical investigations are carried out by considering the experimental study achieved by Hunter [25] on a convergent–divergent of a flat nozzle to simulate the interaction phenomenon of shock waves. The computational domain is a 2D convergent–divergent nozzle with a section ratio of 1.8 and a divergence half-angle of 11.01°. The length of the divergent part L is equal to 0.0577 m, as shown in Figure 2. After validation, the convergent geometry will be changed to study its impact on the detachment of the boundary layers caused by the shock waves in the divergent part.

3.1 Nozzle geometry

Several studies [26–29] showed that the flow in a nozzle subjected to a wave shock is asymmetrical, especially during the starting or at the stop phases. Hence, in this study, the flow is considered symmetric because we are on an established flow regime, and therefore, only the half geometry is represented with the axe of symmetry in 2D space.

3.2 Computational mesh

Several grids are tested to find the best compromise between the accuracy of the results and computational cost. The selected mesh is a structured model with embedded mesh refinement, as shown in Figure 3. The total number of cells is 276,118 cells. It is refined at the throat and walls.

The results are compared with those obtained experimentally by Hunter [25] for different NPRs. Figure 4 shows the results from four meshes compared to the experimental data corresponding to NPR = 3.014. The choice of the mesh depends on the precision with which the boundary layer is processed. The commonly used parameter to evaluate this accuracy is $Y+$. As shown in Figure 4, the values of $Y+$ are less than 5 over the entire interaction zone, representing good precision in determining the properties of the boundary layer.

3.3 Boundary conditions

The simulations are performed by CONVERGE CFD software. The boundary conditions are illustrated in Figure 5. A pressure inlet boundary condition is imposed at the inlet of the primary nozzle. Another pressure-far-field type is set on the ambient pressure, and a final boundary condition of the pressure outlet is required at the output of the computational domain. The walls of the nozzle are

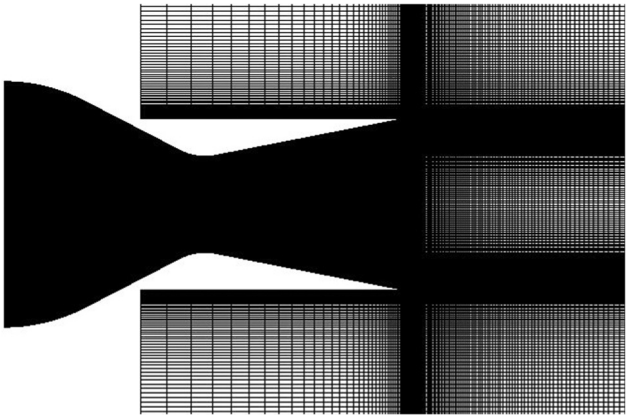

Figure 3: The nozzle structured mesh.

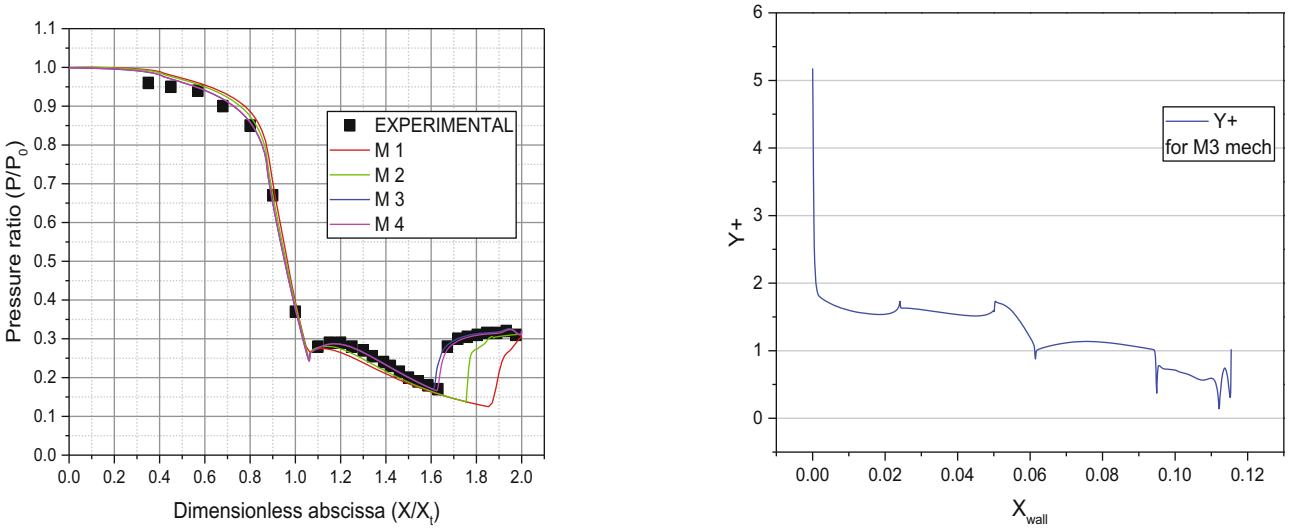

Figure 4: Determination of the best grid mesh for NPR = 3.014 and *Y*+ (*M*3 mesh).

considered adiabatic and symmetry type. These conditions are imposed at the top and the bottom of the computational domain boundaries.

3.4 Turbulence models

In this study, different NPRs are considered: 2.008, 2.412, 3.014, 3.413, 3.816, 4.217, and 5.018. The experimental work reported in ref. [25] corresponds to NPR = 3.014. The choice of the turbulence model can affect the results significantly. The Reynolds-averaged Navier-Stokes approach is adopted as shown in ref. [30], and two turbulence models have been tested in this study, namely, the standard k–ε and k–ω SST models [31]. The results are qualitatively compared to the Schlieren flow visualization, as shown in Figure 6.

As shown in Figure 7, the Mach disk position is apparent with the k–ω SST model, while for the k–ε model, it is in an external position far from the exit. On the other hand, the k–ω SST model accurately follows the boundary layer separation zone compared to the experimental visualization. Furthermore, Figure 8 illustrates the comparison between experimental and numerical nondimensional parietal static pressure of the nozzle. It shows that the pressure decreases more with the k–ε model than with the k–ω SST model at the separation point and daily of the separation point. Consequently, the k–ω SST model will be used in this study.

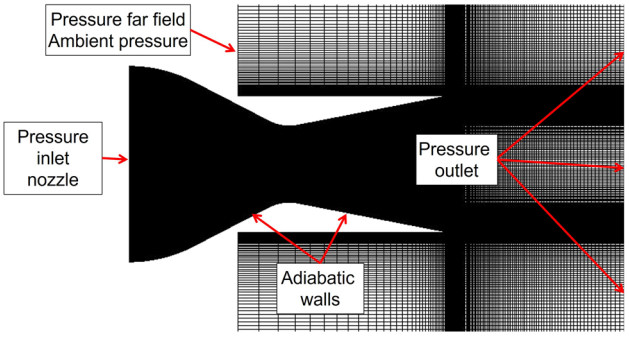

Figure 5: The different boundary conditions.

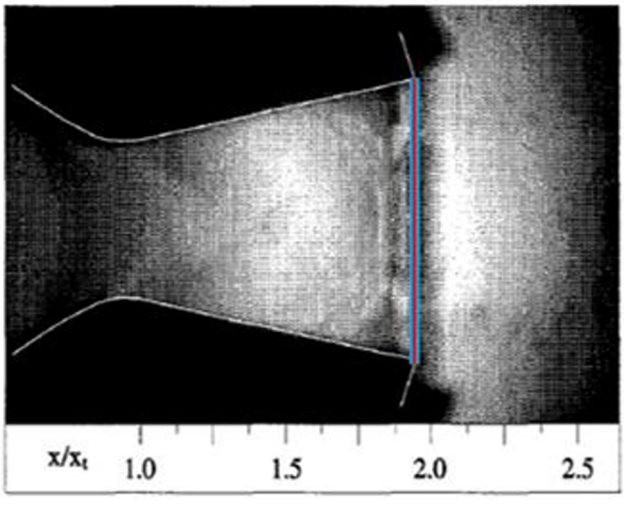

Figure 6: Schlieren flow visualization for NPR = 3.014.

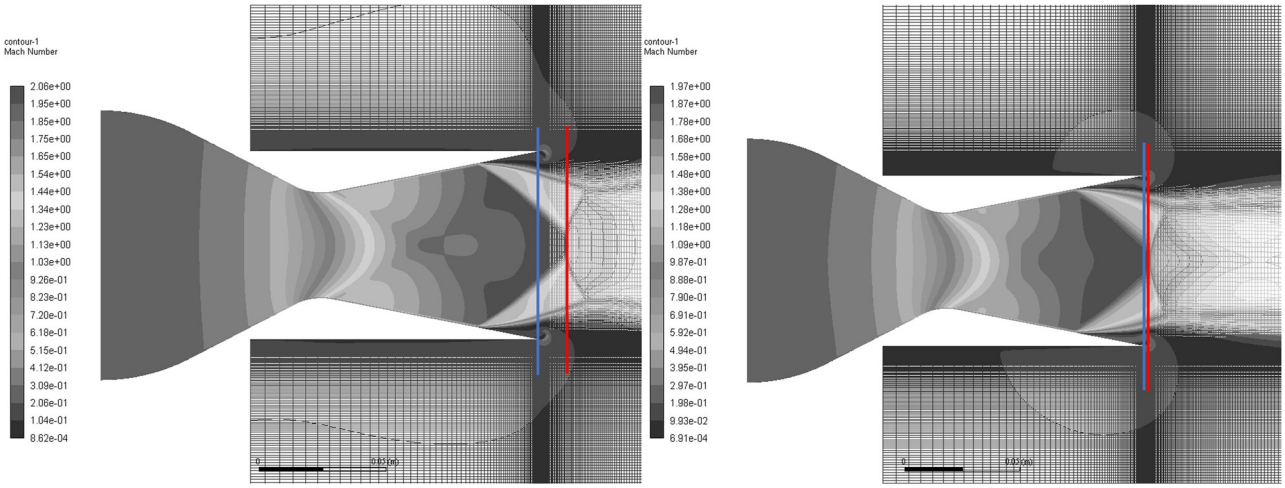

Figure 7: Impact of the two turbulence models on the numerical result: (a) k–ε and (b) k–ω shear-stress transport (SST).

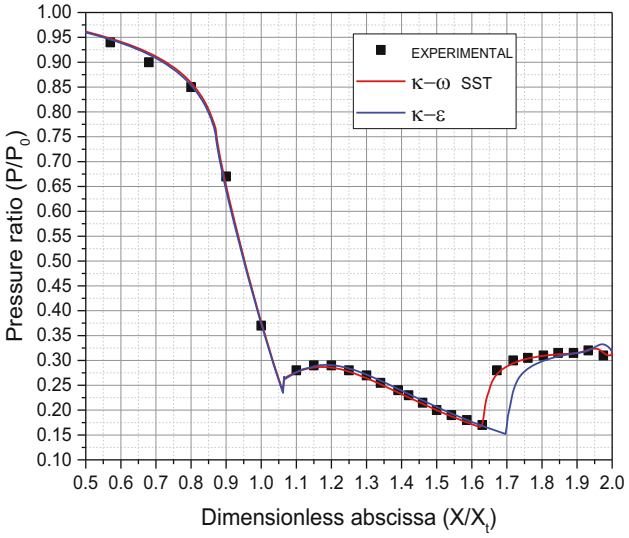

Figure 8: Comparison between the experimental and numerical results of the nozzle parietal static pressure for the two turbulence models.

4 Results and discussion

4.1 Shock tube problem

Ten Fortran programs were used to solve the shock tube problem with 10 different schemes. Reference [21] showed that this problem is numerically sensitive to the selected scheme. Those schemes are tested to choose the best one for describing the shock wave accurately.

They assume that the corresponding ratios are $P4/P1 = 10.0$, $\rho 4/\rho 1 = 10.0$, and $T4/T1 = 1.1$. The Courant–Friedrichs–Lewy number = 0.8. Air is considered a perfect gas with no viscous effect in the 1D flow.

Figure 9 shows that the schemes artificially upstream flux vector splitting (AUFS), advection upwind splitting method (AUSM), ROE, Steger-Warming, VAN-LEER, and Zha-Bligen are in good agreement with the literature [32–39]. Figure 1 shows that the three main zones are captured: the first zone is where the shock wave propagates from high to low pressure, the second zone is where the relaxation wave propagates from low pressure to high pressure, and the third zone is the isobaric line between these two zones. The other schemes, HLLL, LAX, Rusanove, and Ritchmyer, describe more than two different isobar sliding lines [22–24], which is not consistent with the literature.

Figure 10 shows for AUSM and Zha-Bilgne schemes, and this evolution presents oscillations at the isobar line, while the ROE, AUFS, and Steger-Warming schemes offer a solution without numerical oscillations. However, the Steger Warming scheme is noticeably more diffusive.

4.2 Supersonic NASA nozzle

Figure 11 presents the evolution of the pressure ratio P/P_0 (fraction of the parietal pressure on the generative pressure or pressure inlet), according to the nondimensional distance x/xt with xt in throat abscissa. These results

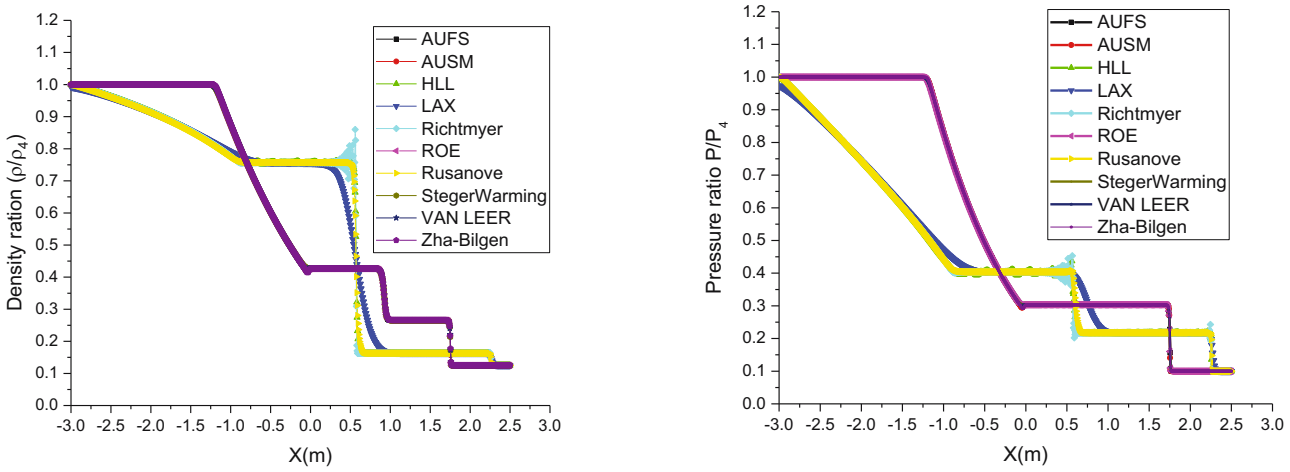

Figure 9: The shock tube problem resolved using different numerical schemes.

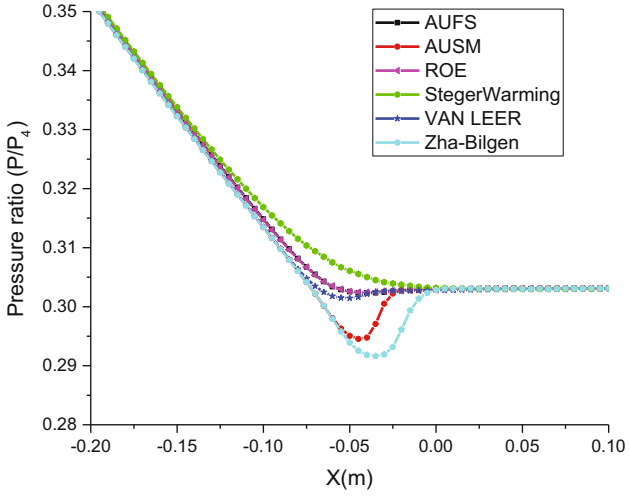

Figure 10: Pressure evolution at isobar line.

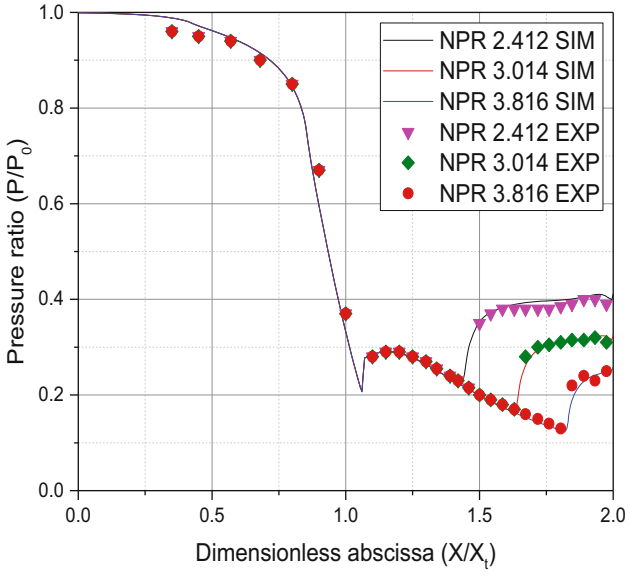

Figure 11: Comparison between numerical and experimental results of parietal static pressures for several NPRs.

correspond to NPR = 2.412, 3.014, and 3.816. They are compared with the experimental results reported in ref. [25] concerning the same NASA nozzle (NASA Langley Research Center 16-Foot Transonic Tunnel complex). Good agreement has been obtained, and we notice that the

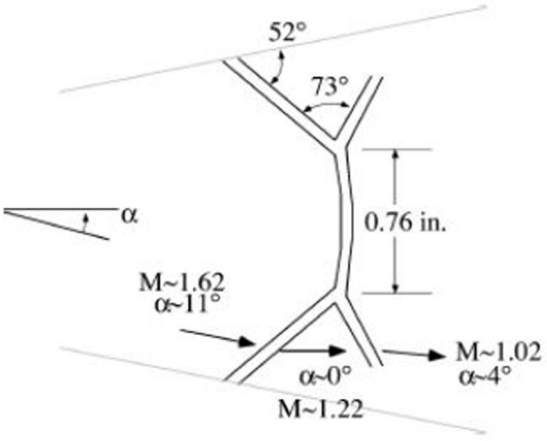

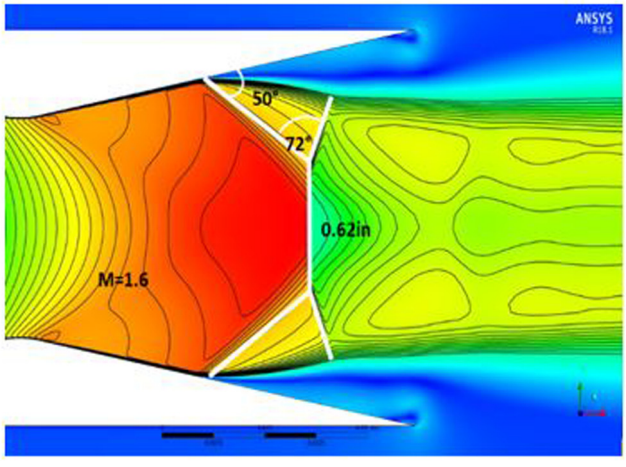

Figure 12: Comparison between numerical and experimental shock scheme for NPR = 2.412.

Profile (A)	Point	X	Y
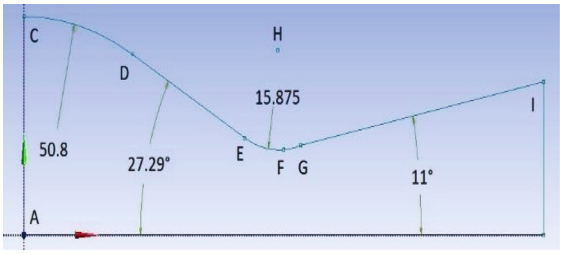	A	0.000	0.000
	B	0.000	-15.596
	C	0.000	35.204
	D	23.292	29.540
	E	50.495	15.519
	F	60.808	14.046
	G	61.722	14.199
	H	57.785	29.616
	I	115.57	24.689

Profile (B)	Point	X	Y
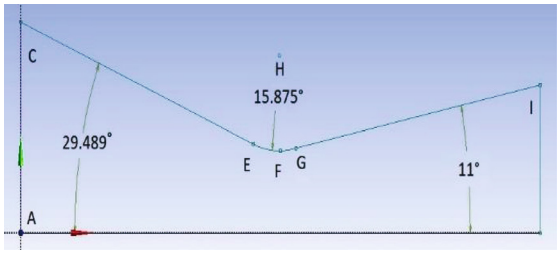	A	0.000	0.000
	C	0.000	35.204
	E	50.495	15.519
	F	60.808	14.046
	G	61.722	14.199
	H	57.785	29.616
	I	115.57	24.689

Profile (C)	Point	X	Y
	A	0.000	0.000
	C	0.000	35.204
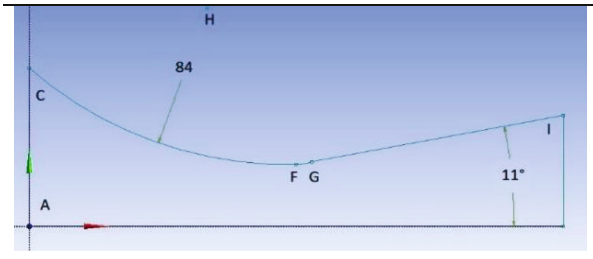	F	60.808	14.046
	G	61.722	14.199
	H	56.1	97.725
	I	115.57	24.689

Figure 13: Geometric profile of the three convergent shapes.

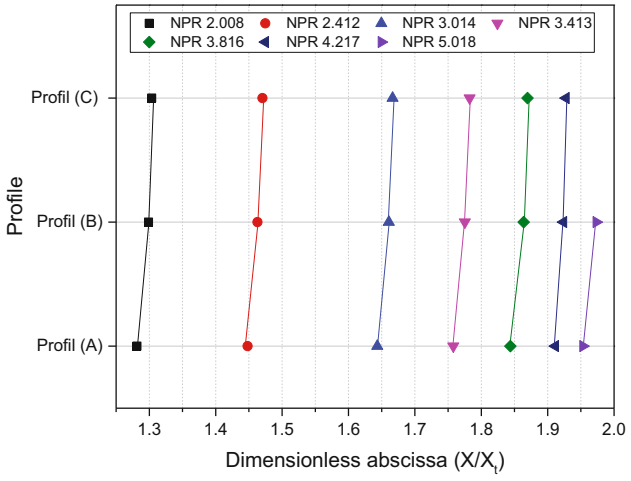

Figure 14: Location of the boundary layer separation for different NPR ratios and convergent profiles.

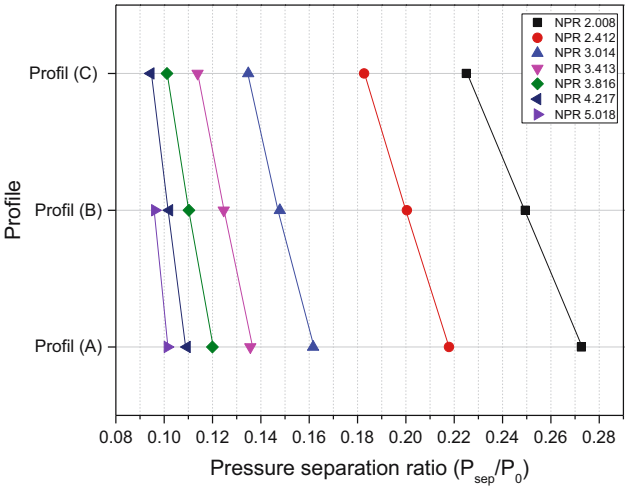

Figure 16: Pressure ratio at the separation point for different NPR and convergent profiles.

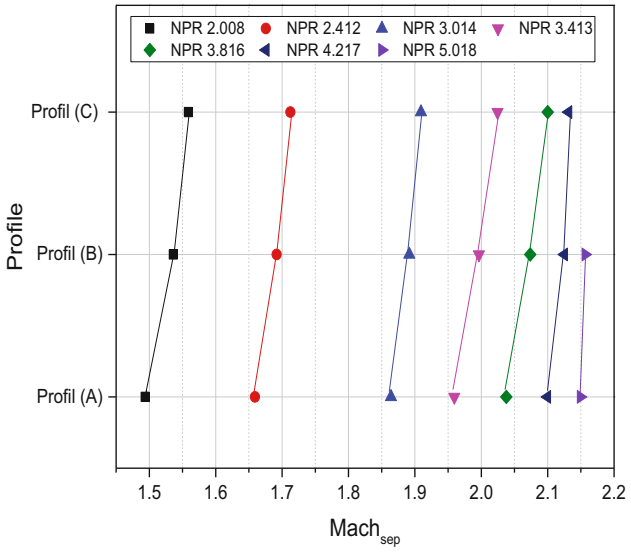

Figure 15: Mach number at separation point for different NPR ratios and convergent profiles.

numerical simulation captures the location of the boundary layer separation. Figure 12 represents the shock scheme case for NPR = 2.412. Although the angles of incident shock and the reflection shock are mostly well simulated, the normal shock length is underestimated with a relative error of 18% compared to the experimental visualization case.

4.3 Impact of the convergent geometry

Some numerical and experimental investigations are focused on the divergent profile impact on the nozzle flow behavior [20,25–31,40]. Still, the effect of convergent remains a gap in the current literature. Hence, we carried out numerical investigations to study the impact of the convergent geometry change on the flow, the coordinates location of the boundary layer separation inside the divergent, and the characteristics of the flow. Three different shapes of the convergent are considered: (i) the convex shape corresponding to the studied nozzle (Profile A), (ii) the conical shape (Profile B), and (iii) the concave shape (Profile C). The input and the output sections of the convergent nozzle of NASA Langley Research Center 16-Foot Transonic Tunnel complex are maintained unchanged. Figure 13 shows the geometric profiles of the three considered convergents.

Figure 14 illustrates the location of the boundary layer separation for each profile. It shows the effect of changing the convergent geometric profile on the appearance of the boundary layer separation. Seven different NPRs ranging from 2.008 to 5.018 are considered. Profile (A) provides an earlier separation location for all NPR values, followed by profile (B). It can be noticed that profile (C) presents the daily point of separation. This behavior is not changing for all NPRs. It can also be seen that profile (C) illustrates the optimum regime behavior for NPR 5.018, which is not the case for the two other profiles (A) and (B).

Figure 15 shows the reached Mach number at the separation section for each profile and each NPR. The results show that the changing of the geometric profile of the convergent influences the Mach number at the separation point called Mach separation. For all NPRs, profile (A) has a lower Mach number than those corresponding to profile (B), and profile (C) provides the higher Mach number separation This difference in Mach number attenuated when the NPR increases and the

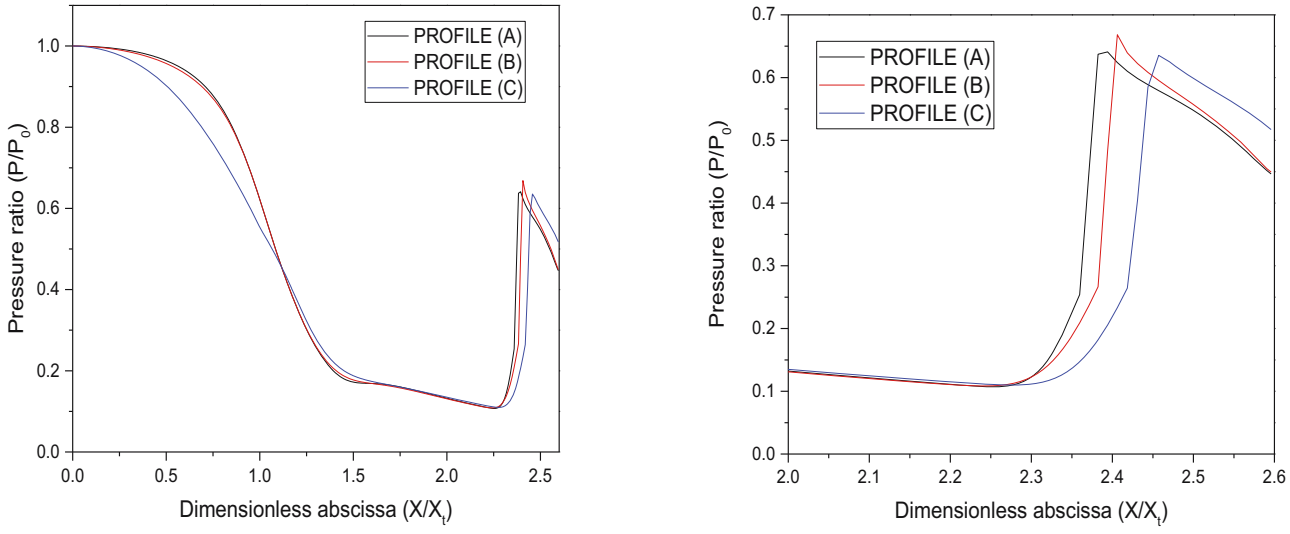

Figure 17: Axial pressure ratio P/P_0 along with the nozzle for different convergent profiles at NPR = 3.816.

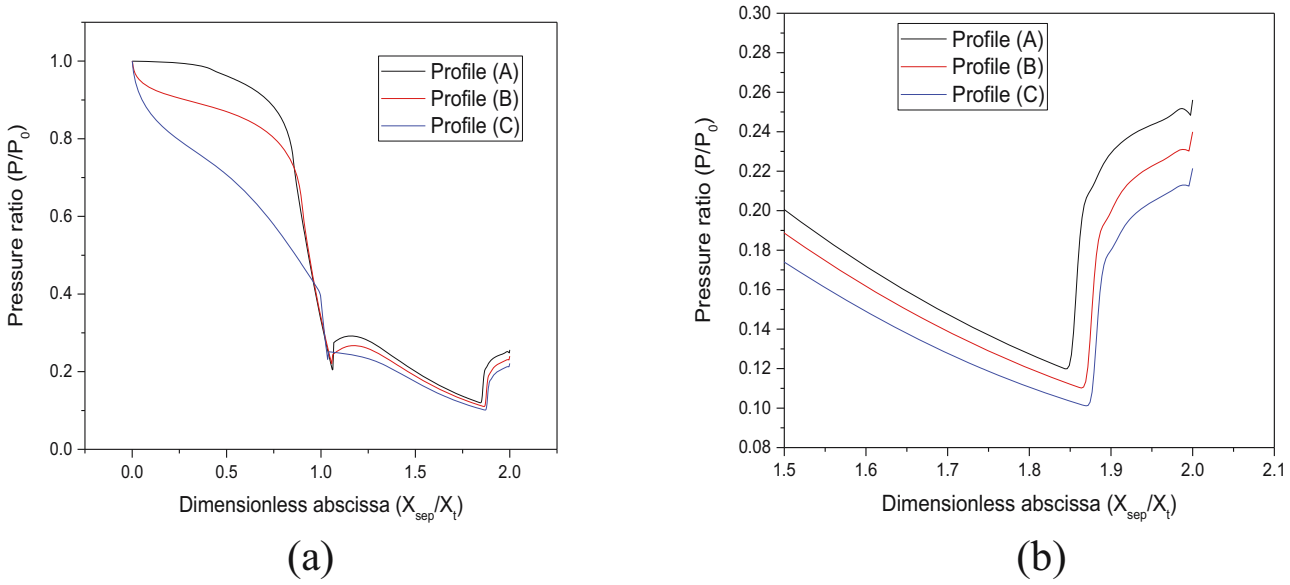

Figure 18: Wall pressure ratio P/P_0 along with the nozzle for different convergent profiles at NPR = 3.816. (a) The evolution of the pressure along the wall of the nozzle and (b) the evolution of the pressure at the separation zone on the wall of the nozzle.

almost same value was obtained at the NPR 5.018, so it can be noticed that profile (C) offers a higher Mach number than the other profiles, and this comportment does not change for all NPRs.

Figure 16 illustrates the different pressure separation ratio at various NPRs. It can be noticed that the lower pressure ratio (P_{sep}/P_0) was always generated on profile (C), which is in good agreement with the result shown in Figure 15. Indeed, the pressure decrease causes the velocity to increase and, consequently, increases the Mach number. For all NPRs, profile (A) has a higher-pressure separation ratio than other profiles (B) and (C). But almost the same results were noticed at NPR 5.018 for (A) and (B). For profile (C), the nozzle is in the optimum regime.

Figure 17 describes the axial evolution of the pressure ratio P/P_0 according to the nondimensional abscissa x/xt. The examination of these curves shows that in graph (a), the pressure curve corresponding to profile (C) decreases more rapidly (strong expansion) between the inlet of the convergent and the throat section than in the other profiles. This effect is due to the impact of the convergent profile, imposing the intensity to decrease along the

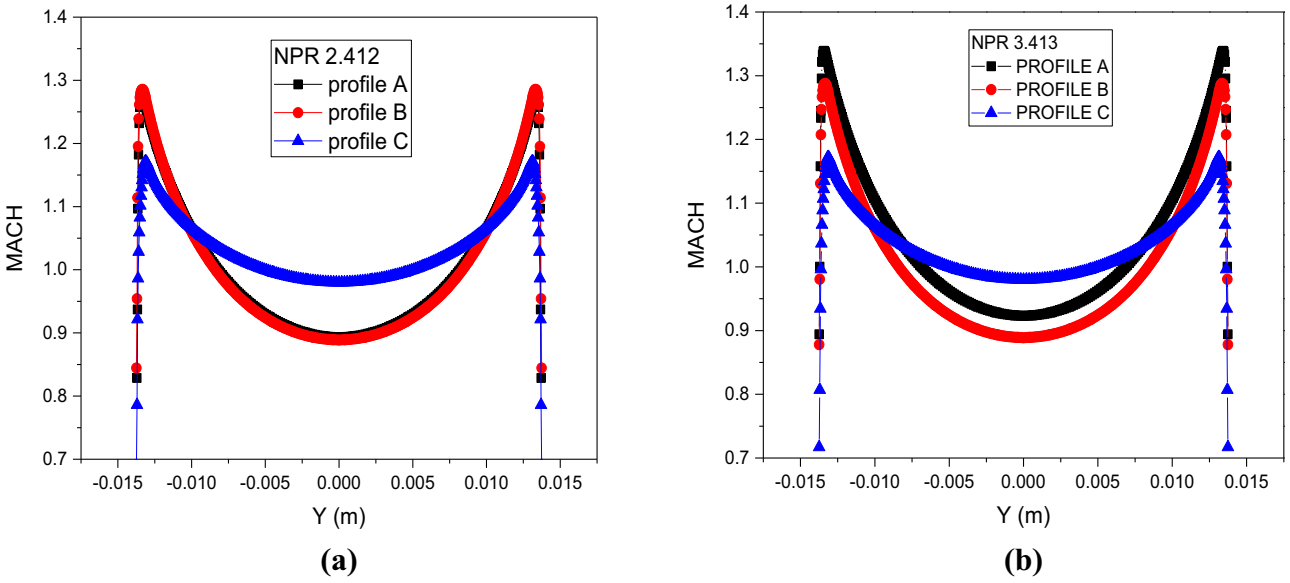

Figure 19: Comparison between the Mach number profile at the throat section for (a) NPR = 2.412 and (b) NPR = 3.413 of different profiles.

abscissa x. For graph (b), the shock wave of profile (C), which recompresses the flow outside the nozzle, is 5% higher than the other profiles. However, the shock wave location is different for each convergent profile. Figure 18 describes the pressure ratio P/P_0 close to the wall according to the nondimensional abscissa x/xt. Similarly, this parietal pressure ratio decreases strongly for profile (C) according to the reduced abscissa x/xt. The ratio P/P_0 is the same at the throat section for all the profiles (sonic wall).

Figure 19 shows the difference between Mach number profiles at the throat section for different NPR and three different convergent profiles. It can be noticed that at the low NPR of 2.008, profiles (A) and (B) are mostly superimposed, and profile (C) is relatively different. The Mach gradient in this section (difference between the highest value and the lower value of Mach) is more important in the case of profiles (A) and (B) with Δ Mach number = 0.4. While for profile (C), Δ Mach number = 0.2. Also, for a higher NPR, Mach number = 3.413. This behavior is confirmed, and the distinction between profiles (A) and (B) are noticed but with the same gradient Δ Mach number = 0.4. For profile (C), Δ Mach number = 0.15, the velocity

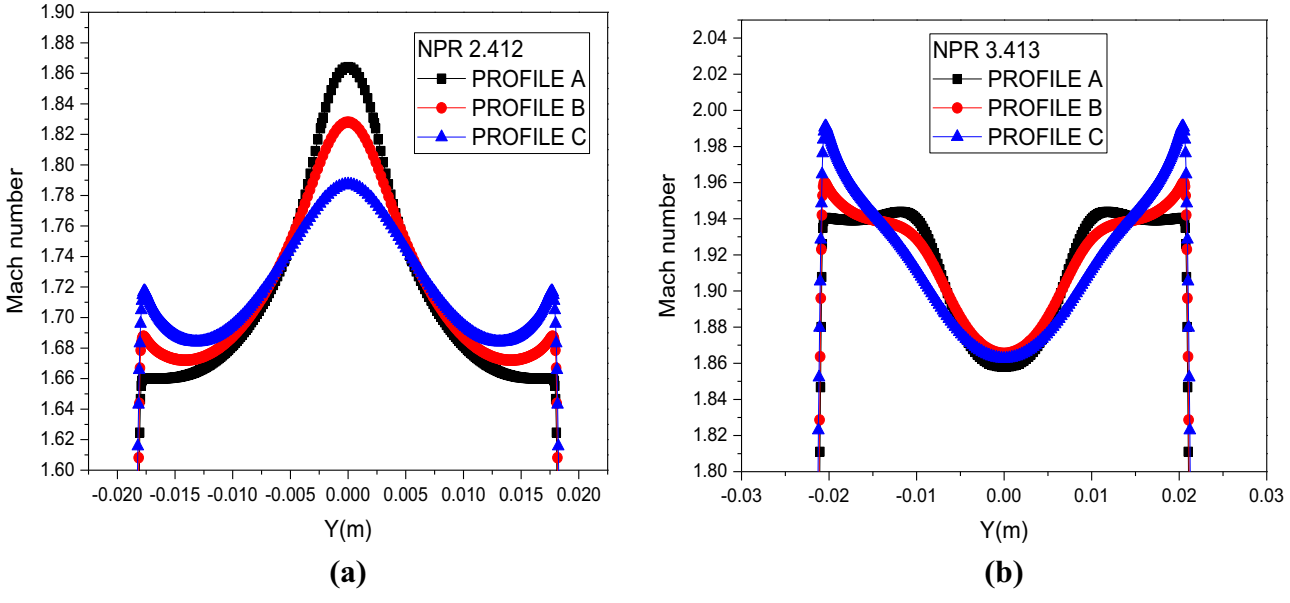

Figure 20: Comparison between the Mach number profile at the separation section for (a) NPR = 2.412 and (b) NPR = 3.413 for different profiles.

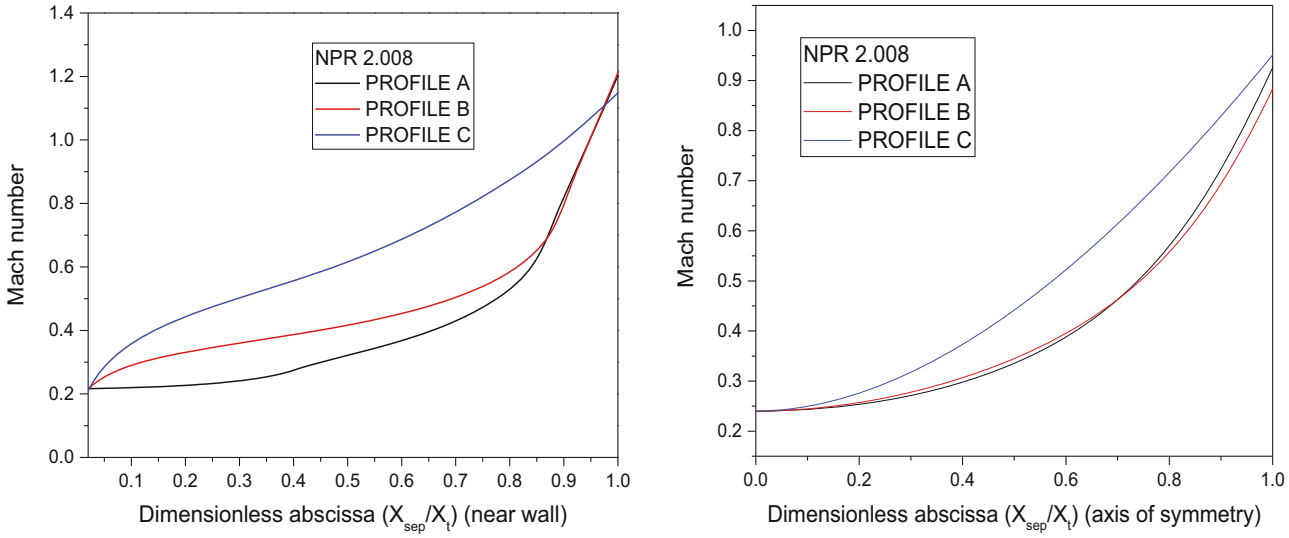

Figure 21: Evolution of the Mach number in the convergent for NPR 2.008.

profile is one of the conditions that create different flow behavior at the downstream (divergent) for different profiles of convergent. At the same time, the Mach number near a wall is always higher in the case of profile (A) followed by (B) and profile (C), and that is true for all NPR. But, at the axis of the flow (axis of the nozzle), the Mach number at profile (C) is higher than profile (A) et (B). This behavior and tendency are reversed in the separation section, as shown in

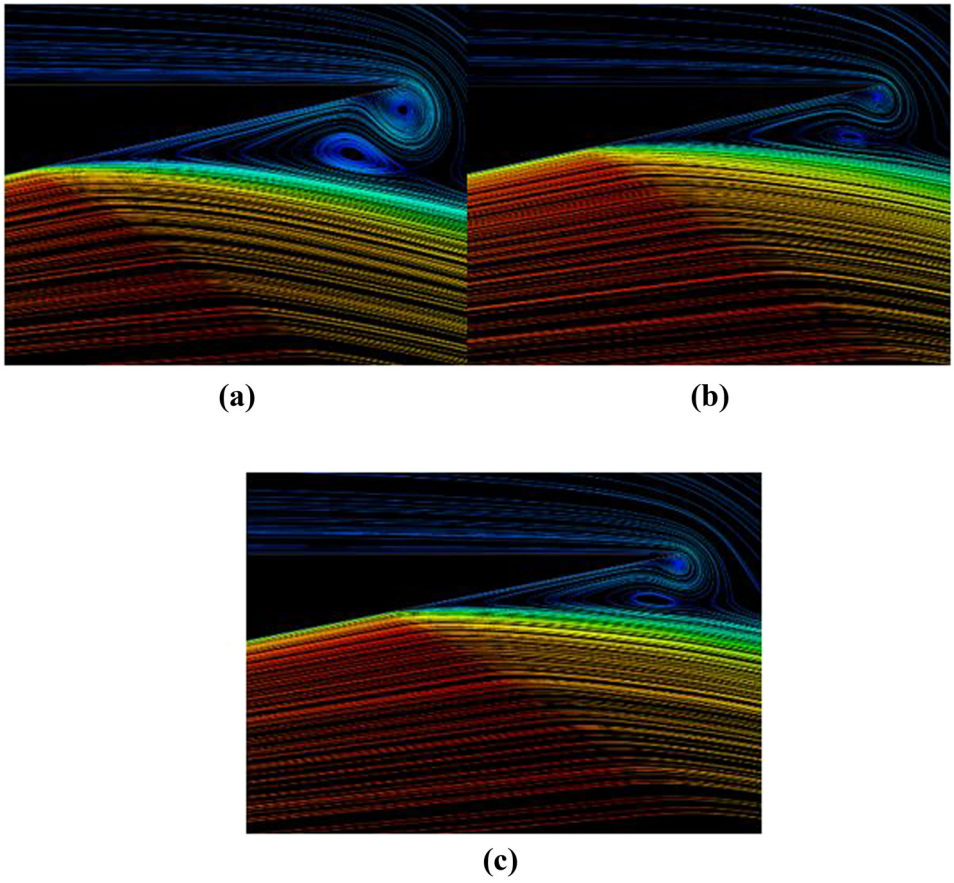

Figure 22: Recirculation zone for profiles a, b and c at NPR = 3.413.

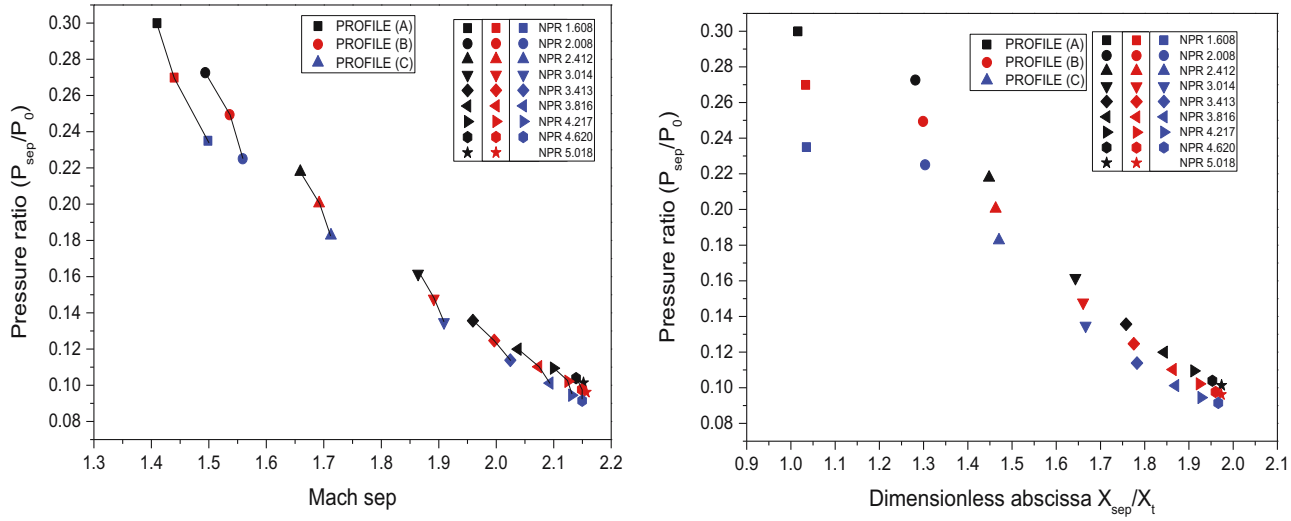

Figure 23: Effect of the convergent geometric profiles on the Mach number, the wall pressure, and the location of the boundary layer separation.

Figure 20, although for profile (C). The distribution of the Mach number is smooth or with a low gradient Δ Mach number. This behavior should result from the quasi-linear acceleration in the convergent, as shown in Figures 17, 18 and 21.

Figure 21 shows the Mach number evolution near the wall (at 1 mm) and at the axis of symmetry for different profiles (A), (B), and (C) for NPR = 2.008. It is noticed that the acceleration in the convergent follows a different curve for different profiles of convergent geometric. Also, profile (C) allows an almost linear acceleration, unlike profiles (A) and (B). This behavior can explain why the profile of Mach number downstream before separation is more uniform and smoother than the two other profiles (A) and (B).

The recirculation zone located downstream of the separation point results from the reintroduction of ambient air inside the nozzle. Figure 22 illustrates the difference between the recirculation zones for the different profiles at NPR = 3.413. It can be seen clearly that profile (A) induced the largest vortex (+40% compared to profile (B) and +60% compared to profile (C)), given the problems that can be generated by this phenomenon such as the lateral load (side-load). It is very important to understand that the change in the convergent profile can influence the vortex intensity of the recirculation zone.

Figure 23 illustrates the effect of changing the convergent geometric profiles on the Mach number, the wall pressure ratio P/P_0, and the location of the separation of the boundary layer for different NPR values. This figure allows better distinguishing the difference between the three studied convergent profiles and observing each profile's behavior for different NPR values. For all NPR values, profile (C) depicts the lowest wall pressure ratio at the point of boundary layer separation. Consequently, it presents the highest resistance to separation than the other profiles and develops a higher Mach number for all NPRs of this study.

For the other two profiles, profile (B) resists the separation relatively more than profile (A) for all NPRs significantly beyond 3.413.

The insert of the obtained results in Figure 24 shows that the three studied profiles follow the resulting tendency found by previous researchers summarized by Stark [40], but only for the NPR from 2.008 to 3.816 (delimited in the figure by the rectangle). It should be noted that the three profiles follow the Schmucker separation criteria Eq. (7). However, it should also be noted that apparently, the Schmucker criteria do not consider the difference induced by the different geometries of the convergent. Still, it is also unable to describe the evolution of P_{sep}/P_a as a function of M_{sep} for NPR 1.608 and NPR 4.217 at 5.018. For these NPR, the separation is close either to the throat or to the outlet lip of the nozzle. The influence of this cretic location makes the relation P_{sep}/P_a a function of M_{sep} obsolete. Figure 23, which is described by a relation P_{sep}/P_0 according to M_{sep}, which describes this evolution well whatever the number of NPR, it also describes the difference of changes in the convergent geometry.

The thrust efficiency results are shown in Figure 25. The measured thrust ratio F/F_i [41] is plotted and compared with the three curves resulting from the numerical simulation of the three different convergent profiles (A)–(C). The analysis shows that the curves of Figure 25 show that the results of Cf resulting from the simulation follow the

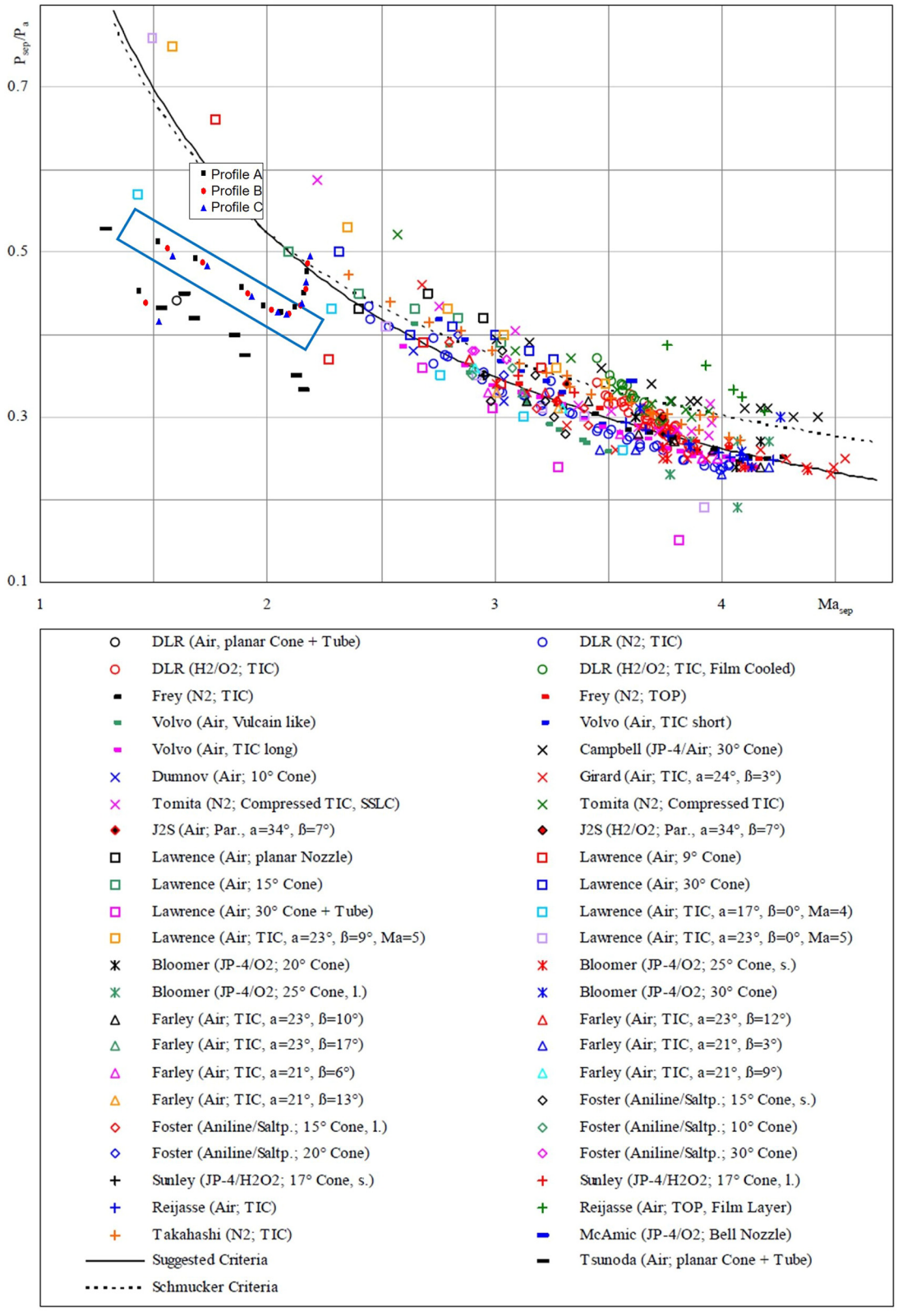

Figure 24: Separation database.

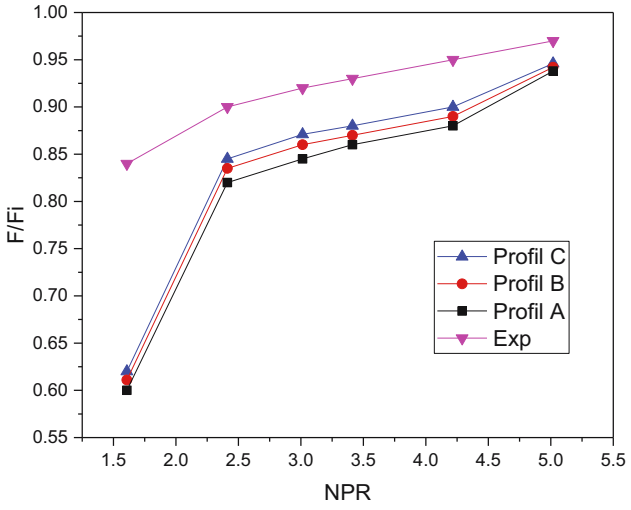

Figure 25: Experimental and numerical thrust efficiency for different profiles and NPR.

experimental results well. This figure also shows that the change in the convergent profile affects the thrust efficiency. We notice that for NPR = 5.016, the three curves of the numerical simulation almost coincide. This NPR represents the optimum regime case, where the separation of the boundary layer is at the nozzle exit lip. For lower NPRs, the curves separate gradually. But, still following the experimental curve tendency, for an NPR of 3.014, profile (C) develops a F/F_i higher than profile (A) by 5%.

5 Conclusion

This work investigated the impact of changes in the convergent geometry profile on the boundary layer separation in an overextended supersonic nozzle numerically. The ROE numerical flow scheme has better predicted the shock wave phenomenon. The following conclusions are drawn from the obtained results.

- The convergent geometric profile of the nozzle impacts the localization of the boundary layer separation and the shock wave because it modifies the profile of velocity and pressure at the throat section.
- The changes in pressure and temperature fields are also due to the convergent geometry change, thus affecting the kinetic energy repartition, potential energy, and the intensity of the Mach, and creating the difference in locations of the boundary layer separation.
- The profiles were adapted well to the Schmucker criterion for NPR, where the separation is far from the exit lip.
- The curve of $P/P_0 = f(M_{sep})$ can give a better criterion. The convergent geometry also influences trust efficiency.

As a recommendation, the geometrical optimization of the nozzles operating in an overextended regime must consider the appropriate geometric profile of the convergent and its impact on the flow behavior.

For future work, our approach will be based on two main objectives:

1) To investigate the optimal convergent geometry profile for nozzle,
2) to expand the simulations on other cases to obtain the maximum data to develop a new boundary layer separation criterion that takes into account the change in the profile of the convergent.

Acknowledgments: The authors wish to express their deep consideration to Convergent Science (USA) team for their cooperation and assistance.

Funding information: The authors state no funding involved.

Author contributions: All authors have accepted responsibility for the entire content of this manuscript and approved its submission.

Conflict of interest: The authors state no conflict of interest.

References

[1] Assonitis A, Paciorri R, Bonfiglioli A. Numerical simulation of shock boundary layer interaction using shock fitting technique. Conference of the Italian Association of Theoretical and Applied Mechanics. Springer; 2019. p. 124–34.
[2] Das BD, Sardar R, Sarkar S, Manna NK, editors. Compressible flow through convergent–divergent nozzle. Singapore: Springer Singapore; 2021.
[3] Zhang Y, Ma Z, Zou J, Zheng Y, editors. Shock bifurcation phenomenon in the reflected shock/boundary layer interaction. Singapore: Springer Singapore; 2019.
[4] Matheson MA, Grosvenor AD, Zheltovodov AA. Shock wave/turbulent boundary layer interactions. Proceedings of the 2011 companion on High Performance Computing Networking, Storage and Analysis Companion. Seattle, Washington, USA: Association for Computing Machinery; 2011. p. 131–2.
[5] Lee C, Choi K, Kim C, Han S. Computational investigation of flow separation in a thrust-optimized parabolic nozzle during high-altitude testing. Comput Fluids. 2020;197:104363.
[6] Goncalves E, Lehnasch BG, Herpe CJ, editors. Hybrid RANS/LES Simulation of Shock-Induced Separated Flow in Truncated

Ideal Contour Nozzle. 31st International Symposium on Shock Waves 2 ISSW 2017 Springer. Cham: Springer International Publishing; 2019.
[7] Li Y, He C, Li J, Miao L, Gao R, Liang J. Experimental investigation of flow separation in a planar convergent-divergent nozzle. Phys: Conf Ser. 2019;1300(1):012088.
[8] Wang YS, Xu JL, Huang S, Lin YC, Jiang JJ. Experimental and numerical investigation of an axisymmetric divergent dual throat nozzle. Part G: J Aerosp Eng. 2020;234(3):563–72.
[9] Léger L, Zmijanovic V, Sellam M, Chpoun A. Experimental investigation of forced flow regime transition in a dual bell nozzle by secondary fluidic injection. Int J Heat Fluid Flow. 2021;89:108818.
[10] Zebiri B, Piquet A, Hadjadj A, Verma S. Shock-induced flow separation in an overexpanded supersonic planar nozzle. AIAA J. 2020;58(5):2122–31.
[11] Vaisakh S, Muruganandam T. Visualization of over-expanded supersonic wall-jet. Aerosp Sci Technol. 2021;112:106617.
[12] Verma SB, Manisankar C. Origin of flow asymmetry in planar nozzles with separation. Shock Waves. 2014;24(2):191–209.
[13] Yu Y. Over-expanded separation transitions of single expansion ramp nozzle in the accelerating and decelerating processes. Aerosp Sci Technol. 2020;98:105674.
[14] Martelli E, Saccoccio L, Ciottoli P, Tinney C, Baars W, Bernardini M. Flow dynamics and wall-pressure signatures in a high-Reynolds-number overexpanded nozzle with free shock separation. J Fluid Mech. 2020;895:A29. doi: 10.1017/jfm.2020.280.
[15] Ivanov I, Kryukov I. Numerical study of ways to prevent side loads in an over–expanded rocket nozzles during the launch stage. Acta Astronaut. 2019;163:196–201.
[16] Papamoschou D, Zill A, Johnson A. Supersonic flow separation in planar nozzles. Shock Waves Springer. 2009;19(3):171.
[17] Gouidmi H, Beghidja A, Benderradji R. Etude numérique d'une structure de choc Phénomène d'interaction choc/couche limite. Rev des Energ Renouvelables. 2017;20(3):397–413.
[18] Quadros R, Bernardini M. Numerical investigation of transitional shock-wave/boundary-layer interaction in supersonic regime. AIAA. 2018;56(7):2712–24.
[19] Meister L, Burtschell Y, Zeitoun DE. Numerical study of a reactive flow in an over-expanded nozzle: influence of wall temperature and altitude. Méc Ind. 2003;4(4):339–46.
[20] Genin C, Stark R. Side loads in subscale dual bell nozzles. Propuls Power AIAA. 2011;27(4):828–37.
[21] Masatsuka K. I, do Like CFD. Vol. 1. Lulu. com; 2013.
[22] Erturk V, Godwe E, Baleanu D, Kumar P, Asad J, Jajarmi A. Novel fractional-order lagrangian to describe motion of beam on nanowire. Acta Phys Polon A. 2021;140(3):265–72.
[23] Jajarmi A, Baleanu D, Vahid KZ, Pirouz HM, Asad J. A new and general fractional Lagrangian approach: a capacitor microphone case study. Results Phys. 2021;31:104950.
[24] Soomro A, Qureshi S, Shaikh AA. A New Nonlinear Hybrid Technique with fixed and adaptive step-size approaches. Sigma J Eng Nat Sci. 2022;40(1):162–78.
[25] Hunter CA. Experimental investigation of separated nozzle flows. Propuls Power AIAA. 2004;20(3):527–32.
[26] Xiao Q, Tsai H-M, Papamoschou D. Numerical investigation of supersonic nozzle flow separation. AIAA. 2007;45(3):532–41.
[27] Shigeru M, Kousuke K, Junji N, Md Tawhidul Islam K, Toshiaki S, Heuy Dong K. Effects of supersonic nozzle geometry on characteristics of shock wave structure. Open J Fluid Dyn. 2012;2012:181–6.
[28] Östlund J, Damgaard T, Frey M. Side-load phenomena in highly overexpanded rocket nozzles. Propuls Power AIAA. 2014;20(4):695–704.
[29] Abdol-Hamid KS, Hunter CA. Numerical investigation of flow in an overexpanded nozzle with porous surfaces. Aircraft. 2006;43(4):1217–25.
[30] Asproulias I, Revell A, Craft T, editors. Modelling shock wave/boundary layer interactions using advanced RANS models. International Symposium on Shock Waves Springr. Springer; 2015.
[31] Menter F. Zonal two equation kw turbulence models for aerodynamic flows. American Institute of Aeronautics and Astronautics AIAA; 1993. p. 1–21.
[32] Hadjadj A. Analyse physique et simulation numérique des écoulements compressibles. Application aux tuyères de propulseurs: Universite de Rouen; 1997. p. 82.
[33] Houas L, editor. Ten Years of shock tube research at Marseille. International Symposium on Shock Waves. Springer; 2013. p. 11–8.
[34] Aune V, Fagerholt E, Langseth M, Børvik T. A shock tube facility to generate blast loading on structures. Int J Protect Struct. 2016;7(3):340–66.
[35] Dewey JM. Explosive flows: shock tubes and blast waves. Handbook of flow visualization. Routledge; 2018. p. 495.
[36] Zhai Z, Zou L, Wu Q, Luo X. Review of experimental Richtmyer–Meshkov instability in shock tube: from simple to complex. Mech Eng Sci. 2018;232(16):2830–49.
[37] Kiverin A, Yakovenko I. Ignition and detonation onset behind incident shock wave in the shock tube. Combust Flame. 2019;204:227–36.
[38] Nativel D, Cooper SP, Lipkowicz T, Fikri M, Petersen EL, Schulz C. Impact of shock-tube facility-dependent effects on incident-and reflected-shock conditions over a wide range of pressures and Mach numbers. Combust Flame. 2020;217:200–11.
[39] Sembian S, Liverts M. On using converging shock waves for pressure amplification in shock tubes. Metrologia. 2020;57:035008.
[40] Stark R, editor. Flow separation in rocket nozzles, a simple criteria. 41st AIAA/ASME/SAE/ASEE Joint Propulsion Conference & Exhibit; 2005.
[41] Hunter CA. An approximate theoretical method for modeling the static thrust performance of non-axisymmetric two-dimensional convergent-divergent nozzles. George Washington University; 1995. p. 32.